Retrieval of global magnetospheric ion distributions from high-energy neutral atom measurements made by the IMAGE/HENA instrument

R. DeMajistre, E. C. Roelof, P. C:son Brandt, and D. G. Mitchell
Applied Physics Laboratory, Johns Hopkins University, Laurel, Maryland, USA

Received 17 November 2003; revised 23 January 2004; accepted 23 February 2004; published 21 April 2004.

[1] In this work we present a method for retrieving global magnetospheric ion distributions from energetic neutral atom measurements made by the IMAGE/HENA instrument. The technique itself is based on the well-established method of constrained linear inversion. In addition to presenting the technique itself, we present a self-consistent method for its optimization. The combination of the technique itself and the tuning process provides a direct measure of the fidelity of the resulting retrievals. We apply these techniques to a representative HENA image and show that the retrieval indeed quantifies the global magnetospheric ion distributions. *INDEX TERMS:* 2794 Magnetospheric Physics: Instruments and techniques; 2778 Magnetospheric Physics: Ring current; 2730 Magnetospheric Physics: Magnetosphere—inner; 2720 Magnetospheric Physics: Energetic particles, trapped; *KEYWORDS:* IMAGE/HENA, energetic neutral atoms, retrievals

Citation: DeMajistre, R., E. C. Roelof, P. C:son Brandt, and D. G. Mitchell (2004), Retrieval of global magnetospheric ion distributions from high-energy neutral atom measurements made by the IMAGE/HENA instrument, *J. Geophys. Res.*, *109*, A04214, doi:10.1029/2003JA010322.

1. Introduction

[2] Energetic neutral atom (ENA) imaging is currently establishing itself as a powerful method for global characterization of the Earth's magnetosphere. The IMAGE spacecraft is now carrying a payload of dedicated ENA instruments (LENA, MENA, and HENA) that have the capability of acquiring ENA imagery over a very broad range of energies. Each image contains information about a large portion of the inner magnetosphere, in contrast to charged particle measurements which are essentially in situ measurements. The power of ENA imaging has been recognized for several years (for example, see *Roelof* [1987]), but with the launch of IMAGE, its utility is now being more fully demonstrated.

[3] Each ENA image contains a great deal of information about the magnetosphere, specifically about the ion distributions that serve as a source of ENA flux via charge exchange in the geocorona and near the Earth's exobase. The information in the images, however, can be difficult to interpret directly without substantial experience. Clearly, quantitative techniques for extracting and presenting this information is required for ENA images to be truly useful.

[4] Over the past few years, several authors have made significant progress in extracting this information from ENA images. *Roelof and Skinner* [2000] presented a nonlinear parametric retrieval algorithm for the extraction of ion distributions. This method makes use of global functions representing the shape of the ion distribution in the magnetosphere. The free parameters of these functions are used in a nonlinear least squares fitting algorithm to provide an optimal fit to the data. The basic limitation of this method is that with a reasonable number of free parameters (e.g., 32), the parametric model is still not able to reproduce all possible shapes that the actual ion distributions can take.

[5] Another approach, which is similar in character to the one use in this work, has been described by *Perez et al.* [2000] and *Perez et al.* [2001]. This method uses cubic B-splines as local basis functions in a constrained linear retrieval. This technique has resulted in reasonable retrievals of both simulations and measured imagery (*Perez et al.* [2000] and *Perez et al.* [2001], respectively), though a systematic analysis of the accuracy of the results has not been published. Our work differs from that of *Perez et al.* [2001] in two important ways. First, we incorporate the effects (such as the angular response function) of the HENA instrument directly into the retrievals. This eliminates much of the systematic error in the retrievals that arise from instrument effects. Second, we have adopted a lower order (linear) set of basis functions. In adopting a linear scheme, we have allowed for a wider range of spatial structure and have simplified the construction of different types of constraints (or so called penalty functions).

[6] In section 2 we give a brief description of the HENA measurements. We develop the basic equations governing these measurements in section 3. Images simulated using the measurement equations are shown in section 4. Our retrieval method is developed and evaluated

0148-0227/04/2003JA010322$09.00

in section 5. Results of the HENA retrievals are compared with in situ measurements in the companion paper, *Vallat et al.* [2004].

2. HENA Measurements

[7] The HENA instrument is aboard the IMAGE spacecraft, which is in an eccentric near-polar orbit (1000 km × 7 R_E altitude). IMAGE is a spin-stabilized platform, whose spin axis is normal to the plane of the orbit with a nominal spin period of 2 min (see *Gibson et al.* [2000] for a more detailed description of the IMAGE spacecraft). The HENA instrument collects energetic neutral atoms (ENAs) from roughly 20 to 200 KeV in a solid angle of 120° by 90°. The instrument is mounted such that the center of the 120° dimension lies in the orbital plane (i.e., perpendicular to the spin axis). Thus in the course of a single spin, the instrument views a 120° by 360° segment of the sky. See *Mitchell et al.* [2000] for a more detailed description of the HENA instrument. ENAs measured during a spin period are separated into energy channels and placed in spatial bins that are regular in the elevation (ϵ) and azimuth (β) angles described in Figure 1.

[8] For energies below 60 KeV the images have a pixel size of roughly 6° × 6°. At higher energies the pixels are 3° × 3° since the spatial spreading caused by the foil is smaller at higher energies. The HENA instrument counts individual ENAs and under most circumstances has a negligible background count rate. For this reason we assume that the measurements in each pixel obey Poisson counting statistics, i.e., we estimate the measurement uncertainties as the square root of the counts without first subtracting an offset.

3. Equations of Measurement

[9] The counts in each pixel of an ENA image, C_i, can be represented by the measurement equation

$$C_i = \int_{\Delta t}\int_{\Delta E}\int_0^{2\pi}\int_0^{\pi} [A_i(\epsilon,\beta,E,t)] j_{ena} \sin\epsilon d\epsilon d\beta dE dt, \quad (1)$$

where A_i is the response of the pixel i to an ENA intensity j_{ena} at time t, energy E, and angular position ϵ and β. Note that the instrument response function, A_i, is written in a fairly general form to account for spatial, temporal, and energy spreading. As we shall see below, spatial spreading is particularly important for HENA measurements. Although the HENA images are sampled in 6° × 6° (or 3° × 3°) degree bins, the instrument spreading can be significantly larger. The ENA intensity from charge exchange can be written as

$$j_{ena} = \int_0^{s_e} n^H(s)\sigma_H^{10}(E) j_{ion}(s,E) ds + j^e_{ena}(s_e), \quad (2)$$

where s is the distance along the line of sight determined by ϵ and β, n^H is the number density of hydrogen, σ_H^{10} is the charge exchange cross section for protons on hydrogen, and j_{ion} is the ion intensity. The notation for the cross section σ_H^{ij} refers to the transition from a charge state of i to a charge state of j (thus the stripping cross section would be σ_H^{01}). The limit of integration, s_e, is either the point where the line of sight first intersects the exobase or $+\infty$ for lines of sight with no such intersection. In writing equation (2) we have separated the ENA intensity into two distinct components, the optically thin geocorona and the optically thick emission from the region near the exobase, $j^e_{ena}(s_e)$, as described by *Roelof* [1987]. In the geocorona we assume charge exchange with hydrogen atoms only. The emission near the exobase is a result of charge exchange with atomic oxygen and is not discussed further in this paper because we only use IMAGE vantage points where its intensity can be neglected. Note that we also neglect the contribution of charge exchange with helium, whose concentration only exceeds that of hydrogen only below 1.24 Earth radii (1500 km) or so.

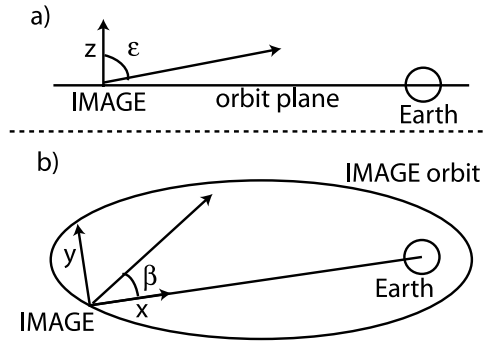

Figure 1. Geometry of HENA observations from (a) within the plane of the orbit and (b) above the plane of the orbit. The x axis points along the vector from the IMAGE spacecraft to the center of the Earth and the z axis points in the direction of the spacecraft spin axis. The angles ϵ and β are the polar and azimuthal angles in this system.

[10] The counts from geocoronal emissions can be expressed as

$$C_i = \int_0^{2\pi}\int_0^{\pi}\int_0^{s_e} n^H \sigma_H^{10} \langle A_i(\epsilon,\beta)\rangle j_{ion} ds \sin\epsilon d\epsilon d\beta, \quad (3)$$

where we have made the substitution

$$\langle A_i(\epsilon,\beta)\rangle = \int_{\Delta t}\int_{\Delta E} A_i(\epsilon,\beta,E,t) dE dt. \quad (4)$$

In making this substitution we have assumed that a particular pixel, i, has been collected for a brief interval of time Δt and a narrow energy range ΔE and that these intervals are suitably narrow that j_{ena} can be considered constant over them. The instrument function $\langle A_i(\epsilon, \beta)\rangle$ appropriate for HENA is based on the description in the work of *Mitchell et al.* [2000].

3.1. Description of the Ion Intensity

[11] In all that follows we assume that over the collection time Δt, the ion intensity, j_{ion}, can be uniquely represented in a nonorthogonal dipole based coordinate system, i.e.,

$$j_{ion} = j_{ion}\left(L,\phi,\mu_{eq}\right). \quad (5)$$

This system is closely related to the Solar Magnetic coordinate system [*Russell*, 1971] represented in the spherical coordinates (r, θ, ϕ). In the dipole representation $r = L\sin^2\theta$ (measuring distance in earth radii R_e) and μ_{eq} is the cosine of the angle of the velocity vector to the field line (the so-called pitch angle cosine) at the equator. In writing equation (5) we have assumed that the ions obey the adiabatic invariants, that is, the ions are constrained to follow field lines and that the pitch angle cosine at any point in an ion's trajectory can be determined from its equatorial pitch cosine, μ (the first adiabatic invariant), by

$$1 - \mu^2 = \frac{B(\theta)}{B(\pi/2)}\left(1 - \mu_{eq}^2\right) \tag{6}$$

or exploiting the dipole shape of the magnetic field

$$\mu^2 = 1 - \left(1 - \mu_{eq}^2\right)\frac{\sqrt{1 + 3\cos^2\theta}}{\sin^6\theta}, \tag{7}$$

where $B(\theta)$ is the magnitude of the magnetic field (at constant L) for a given θ. Since the pitch angle distribution is symmetric about zero, j_{ion} is determined for all values of θ if $j_{ion}(\mu_{eq})$ is known for $0 \le \mu \le 1$.

[12] Another important feature of j_{ion} is the possible presence of a depleted loss cone. Ions that mirror at or below the exobase are quickly removed from the distribution by charge exchange. The mirror altitude at a fixed L can be regarded as a function of the equatorial pitch angle μ_{eq} The point at which the mirror radius is equal to the exobase radius, R_{atm}, defines the equatorial loss cone pitch angle cosine [see *Lyons and Williams*, 1984]

$$\mu_{eqlc}^2 = 1 - \frac{R_{atm}^3}{L^3}\frac{1}{\sqrt{4 - 3R_{atm}/L}}. \tag{8}$$

If a loss cone is present, the ion intensity, $j_{ion}(L, \theta, \mu_{eq})$, will be depleted where $\mu_{eq} \ge \mu_{eqlc}$. The existence and depth of the loss cone depends on the source of the ion intensity and cannot be predicted a priori.

[13] In view of the above discussion we have found it convenient to parameterize the pitch angle distribution as follows:

$$j_{ion}\left(L, \theta, \mu_{eq}\right) = U\left(\mu_{eq}, \mu_{eqlc}(L), m\right)\sum_{p=0}^{N} j_{ion}^{(p)} P_p^*\left(\mu_{eq}\right), \tag{9}$$

where the functions $P_p^*(\mu_{eq})$ are the Legendre polynomials scaled to the interval (0, 1) and the parameter m is set to 1 if the loss cone is present or 0 if is not. The function $U(\mu_{eq}, \mu_{eqlc}(L), m)$ is a binary function that is zero if $\mu_{eq} > \mu_{eqlc}(L)$ and $m = 1$ and equal to 1 otherwise. The U function therefore governs the behavior of the loss cone, which is considered either completely filled ($m = 0$) or completely empty ($m = 1$). Clearly, the number of pitch angle moments, N, determines the amount of detail in the pitch angle structure that can be represented by equation (9).

[14] In this subsection we have constrained the behavior of the ion intensity function j_{ion} by choosing an explicit representation and dependencies for it. We have assumed that over the period of observation (2 min) the motion of the ions is dominated by a dipole magnetic field. All other forces, e.g., electric fields, act on significantly longer timescales and are therefore negligible. Further, we have neglected all perturbations of the dipole field. This may lead to errors for larger values of L (greater than 6 or so), particularly when the magnetosphere is stretched. The overall effect of such a bias will be to incorrectly assign ion fluxes to smaller values of L.

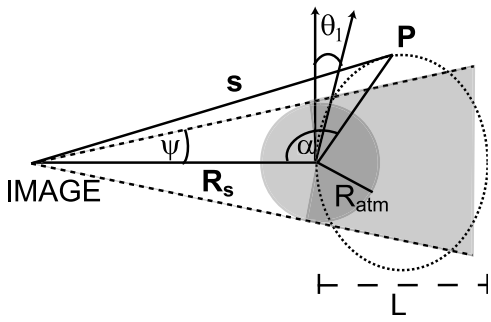

Figure 2. Obscuration of volume elements. For an observer at IMAGE, located at a position $\mathbf{R_s}$, viewing a volume element at **P** along line of sight **s**. The line of sight to **P** is obscured if it lies in any of the grey areas. The dotted curve represents the field line with an equatorial distance L. The angle $\theta_1 = \arcsin\left(\sqrt{R_{atm}/L}\right)$ is the polar angle where the northward L contour intersects with the exobase (located at radius R_{atm}). The dashed rays originating from IMAGE represent the tangent cone. That is, the cone described by rays originating from the IMAGE spacecraft that have a distance of closest approach to the Earth equal to R_{atm}.

3.2. Geocoronal Emission

[15] The geocoronal component of the measurement, equation (3), can be viewed as a volume integral over all space above the exobase that is not obscured by the Earth. This integral can be expressed in terms of (L, θ, ϕ) through the introduction of the Jacobean

$$J_0(L, \theta, \phi) = \sin^3\theta\frac{r(L, \theta)^2}{s(L, \theta, \phi)^2}. \tag{10}$$

[16] Before rewriting equation (3) in terms of these new variables, the limits of the integration must be determined as well. Equation (3) can be recast as a integral over all space through the introduction of an obscuration function O which has the value of 1 or 0 if the specified volume element is outside of or inside of the obscuration region, respectively. The geometry of O is shown in Figure 2. The Earth's atmosphere (the lying below the exobase) is the source of the obscuration. Any line of site that passes through the exobase we consider to be obscured for the purposes of the retrieval. First, any volume element that lies below the exobase is obscured. Referring to Figure 2, we see that this region is defined by $\sin\theta < \sin\theta_1$. Further, any volume elements are that are above the exobase are also obscured if they lie on a ray originating at IMAGE that passes through the exobase (i.e., in the tangent cone) and lie beyond the exobase on that ray. These regions are effectively blocked by the Earth and its atmosphere. Note that the volume elements in front of the Earth are not obscured.

Thus referring to Figure 2, volume elements that lie behind the Earth's atmosphere (the condition for which is $\alpha + \psi > \frac{\pi}{2}$) and lie within the tangent cone (which requires $\sin^2\theta \sin(\alpha + \psi) < \sin^2\theta_1$) are obscured. The function O can be written as

$$O(L,\theta,\phi) = \begin{cases} 0 & \text{if } \sin\theta < \sin\theta_1 \\ 0 & \text{if } \alpha+\psi > \frac{\pi}{2} \text{ and } \sin^2\theta\sin(\alpha+\psi) < \sin^2\theta_1 \\ 1 & \text{otherwise.} \end{cases} \tag{11}$$

The condition $\sin\theta < \sin\theta_1$ can be incorporated directly in the limits of integration over both L and θ, as contributions to the integral can only be made where $L > R_{atm}$ and $\theta_1 < \theta < \pi - \theta_1$.

[17] Using equations (9) and (10), equation (3) can be expressed in terms of the natural coordinates of j_{ion} as

$$C_i = \sum_p \int_0^{2\pi} \int_{R_{atm}}^{\infty} f_i^p\left(L,\phi,\mu_{eq}\right) j_{ion}^p(L,\phi) dL d\phi, \tag{12}$$

where

$$f_i^p\left(L,\phi,\mu_{eq}\right) \equiv \sigma_H^{10} \int_{\theta_1}^{\pi-\theta_1} n^H \langle A_i\rangle J_0 O P_p^*\left(\mu_{eq}\right) d\theta. \tag{13}$$

The integral in equation (13) can be calculated numerically via Romberg integration [*Press et al.*, 1988].

[18] Using the techniques developed in Appendix A, equation (12) can be approximated by numerical quadrature as

$$C_i = \sum_p \sum_k \sum_l b_{ikl}^p j_{ion}^p(L_l,\phi_k), \tag{14}$$

where the quadrature weights b_{ikl}^p are determined by integrals of the form (see equation (A8))

$$\zeta_{ikl}^{pnm} = \int_{L_l}^{L_{l+1}} \int_{\phi_k}^{\phi_{k+1}} g_{kl}^{nm} f_i^p dL d\phi \tag{15}$$

with

$$g_{kl}^{nm} = \frac{(-1)^{n+m}(L_{l+m} - L)\left(\phi_{k+n} - \phi\right)}{(L_{l+1} - L_l)\left(\phi_{k+1} - \phi_k\right)}. \tag{16}$$

The integrals in equation (15) are performed by means of the four point integration scheme described by *Abramowitz and Stegun* [1972]. Equation (14) is thus a well-defined, linearized forward model for HENA geocoronal measurements. Equation (14) can be written in matrix form as

$$C = \left|K^0\ K^1\right| \left| \begin{matrix} J_{ion}^0 \\ J_{ion}^1 \end{matrix} \right|, \tag{17}$$

where the superscripts on $\boldsymbol{K}^p$ and $\boldsymbol{J}_{ion}^p$ signify the dependence on the pitch angle moments (see equation (9)).

[19] We can simplify the interpretation of the pitch angle moments, $\boldsymbol{J}_{ion}^p$, if only the first two terms are taken ($p = 0, 1$). Noting that the function $P_p^*(x)$ are the Legendre polynomials scaled to the interval (0,1) so that $P_0^*(x) = 1$, $P_1^*(0) = -1$ and $P_0^*(1) = 1$ and considering only the first two moments, we write

$$\begin{aligned} \sum_{p=0}^{1} j_{ion}^{(p)} P_p^*(0) &= j_{ion}^{(0)} - j_{ion}^{(1)} \\ \sum_{p=0}^{1} j_{ion}^{(p)} P_p^*(1) &= j_{ion}^{(0)} + j_{ion}^{(1)} \end{aligned} \tag{18}$$

we can immediately identify the quantities

$$\begin{aligned} j_{ion}^{\perp} &\equiv j_{ion}^{(0)} - j_{ion}^{(1)} \\ j_{ion}^{\parallel} &\equiv j_{ion}^{(0)} + j_{ion}^{(1)}, \end{aligned} \tag{19}$$

which are the equatorial ion intensities perpendicular ($j_{ion}(\mu = 0)$) and parallel ($j_{ion}(\mu = 1)$) to the field lines, respectively. Equation (17) can now be written in terms of these more intuitive quantities as

$$C = \left|K^{\parallel}\ K^{\perp}\right| \left| \begin{matrix} J_{ion}^{\parallel} \\ J_{ion}^{\perp} \end{matrix} \right|, \tag{20}$$

where we have defined

$$\begin{aligned} K^{\parallel} &= \frac{1}{2}\left(K^0 + K^1\right) \\ K^{\perp} &= \frac{1}{2}\left(K^0 - K^1\right). \end{aligned} \tag{21}$$

Experience with the HENA measurements and retrievals have shown that no more than two pitch angle moments can be resolved. Thus the representation of equation (20) is slightly preferable to that of equation (17). This representation is not only more intuitive, it also allows for the possibility of implementing nonnegativity constraints on the retrievals. This last advantage is due to the fact that in order to be physically acceptable, $\boldsymbol{J}_{ion}^{\parallel}$ and $\boldsymbol{J}_{ion}^{\parallel}$ must be positive, though physical acceptable values of $\boldsymbol{J}_{ion}^{\perp}$ can have either sign.

4. Simulated HENA Images

[20] Before proceeding to inversions, we will use the equations developed in the previous section to simulate HENA measurements. This will provide a groundwork for much of the discussion in the sections relating to constraint tuning and error analysis.

[21] Simulations are based on equation (20), which in turn depends on the construction of the kernel, $\boldsymbol{K}$. In order to calculate the kernel, several quantities must be specified. The geocoronal hydrogen density is based on the DE-1 measurements of *Rairden et al.* [1986] as recently confirmed by the IMAGE measurements of *Østgaard et al.* [2003]. The charge exchange cross section for hydrogen, σ_H^{10}, has been taken from *Barnett* [1990]. We can now

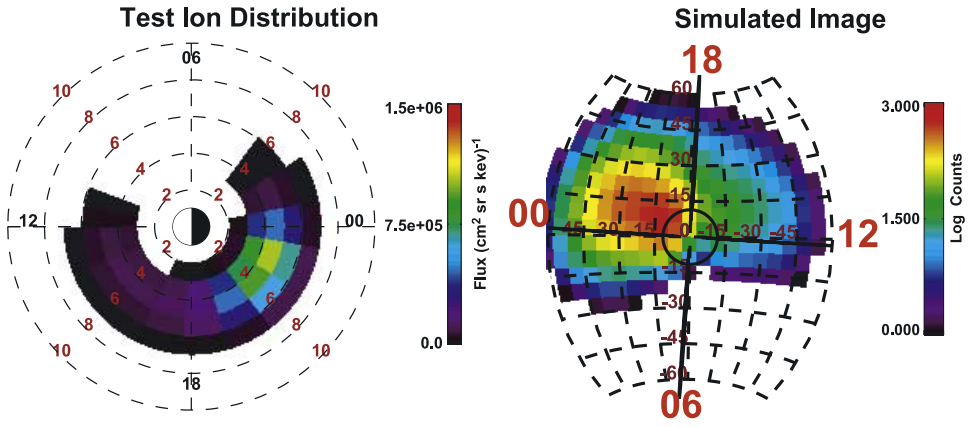

Figure 3. Simulated HENA image (right) using the test equatorial ion distribution (left) based on the actual viewing geometry that occurred on 4 October 2000. The test distribution is described in the text. On the ion distribution panel, the closed dashed curves represent the scale of L (2–12) in Earth radii and the local time scale is given outside of the perimeter of the outermost L boundary. The simulated image is presented in a projection described in detail by *C:son Brandt et al.* [2002]. The dashed black lines on the image represent the values in ϵ and β and the solid black curves show curves of constant L (L = 4, 8) at four local times (which are labeled in red).

calculate the kernel using these quantities, the HENA instrument function and the ion distribution.

[22] Figure 3 shows the results of a simulation of an actual HENA observation that occurred on 4 October 2000 at ~1700 hours UT. This simulated distribution was generated by a trial and error fitting method to the measured data. That is, the ion distribution was adjusted by hand until the HENA image that resulted matched (at least qualitatively) the measured data. Note that we do not assert that this is an actual inferred ion distribution. Rather, it is a physically reasonable distribution that is suitable for testing the behavior of quantitative retrievals. The test ion distribution has a maximum near L = 4 in the midnight-dawn sector. This is reflected in the simulated image which also shows a midnight-dawn enhancement. The viewing perspective, the geocoronal distribution, and the instrument spread function make visual inference of the test ion distribution from the simulated image somewhat difficult. The ENA intensity is a product of the ion distribution and the neutral density, thus for a given field line the maximum ENA intensity will occur where the density is highest, i.e., where the distance to the Earth is smallest. Thus the maximum intensity generally occurs where the ions mirror. For this reason, the peak of the ion density will appear to occur closer to the Earth in the image. Finally, the HENA instrument has a finite spread function; sharp bright areas of the intensity are broadened by the instrument. This is evident in the simulated image where there appears to be significant emission on the sunward side of the Earth. This apparent sunward side emission is, however, due to postmidnight emission spread by the instrument.

[23] From the figure it is clear that the ENA image contains a good deal of information about the ion distribution. The interpretation of this information directly from the image, even qualitatively, can be difficult. It is for this reason that we seek to develop a recovery technique that can reproduce, as far as possible, the ion distribution from the image.

5. Constrained Linear Inversion

5.1. Inversion Equations

[24] In a strict sense, equation (20) can only be solved uniquely if the matrix $\boldsymbol{K}$ is both square and nonsingular. In practice, meeting these two criteria simultaneously is not possible. Instead of seeking a direct solution, we could pursue a least squares solution, i.e., determine $\boldsymbol{J}_{ion}$ through minimizing the quantity

$$(\boldsymbol{C} - \boldsymbol{K}\boldsymbol{J}_{ion})^T \boldsymbol{\sigma}_C^{-2} (\boldsymbol{C} - \boldsymbol{K}\boldsymbol{J}_{ion}), \tag{22}$$

where $\boldsymbol{\sigma}_C^{-2}$ is the inverse of the measurement covariance matrix. For the HENA data, $\boldsymbol{\sigma}_C^{-2}$ is a diagonal matrix whose elements are $1/\sigma_i^2$ with σ_i as the uncertainty corresponding to each pixel. Minimizing equation (22) yields

$$\boldsymbol{J}_{ion} = \left(\boldsymbol{K}^T \boldsymbol{\sigma}_C^{-2} \boldsymbol{K}\right)^{-1} \boldsymbol{K}^T \boldsymbol{\sigma}_C^{-2} \boldsymbol{C}. \tag{23}$$

Unfortunately, in the case of the HENA measurements, the matrix $\boldsymbol{K}^T \boldsymbol{\sigma}_C^{-2} \boldsymbol{K}$ is very poorly conditioned. For this reason, application of equation (23) results in a highly oscillatory solution that is dominated by numerical noise. In spite of the fact that we have more measurements than unknowns, the measurements do not contain enough information to uniquely determine $\boldsymbol{J}_{ion}$ (in the retrievals that follow, there are 600 image pixels and 216 elements of the retrieved ion distribution). We must therefore add information about $\boldsymbol{J}_{ion}$ in the form of a priori constraints. Instead of minimizing the expression (22), we instead minimize

$$(\boldsymbol{C} - \boldsymbol{K}\boldsymbol{J}_{ion}) \boldsymbol{\sigma}_C^{-2} (\boldsymbol{C} - \boldsymbol{K}\boldsymbol{J}_{ion}) + \gamma \boldsymbol{J}_{ion}^T \boldsymbol{H} \boldsymbol{J}_{ion}, \tag{24}$$

where γ is a constant and $\boldsymbol{H}$ is a constraint matrix. Both γ and $\boldsymbol{H}$ will be described in detail below. The result of the minimization is

$$\boldsymbol{J}_{ion} = \left(\boldsymbol{K}^T\boldsymbol{\sigma}_C^{-2}\boldsymbol{K} + \gamma\boldsymbol{H}\right)^{-1}\boldsymbol{K}^T\boldsymbol{\sigma}_C^{-2}\boldsymbol{C}, \tag{25}$$

which for appropriate values of γ and $\boldsymbol{H}$ has a unique solution. Solutions of this form have been treated extensively by other authors [see, e.g., *Twomey*, 1977; *Rodgers*, 2000; *Menke*, 1989]; only a brief summary has been described here.

[25] In the expression in equation (24) the constant γ serves a tuning parameter, determining the relative contribution of the a priori constraints to the solution. As γ becomes larger, the solution is more tightly bound to the constraint. The constraint matrix $\boldsymbol{H}$ can take several forms and is usually written in the form

$$\boldsymbol{H} = \boldsymbol{D}^T\boldsymbol{D}, \tag{26}$$

where $\boldsymbol{D}$ is a linear operator that when applied to $\boldsymbol{J}_{ion}$ is expected to be small. For example, defining $\boldsymbol{D}$ as $\boldsymbol{D}_0$, the identity operator, the constraint in equation (25) would favor solutions with smaller $\boldsymbol{J}_{ion}^T\boldsymbol{J}_{ion}$, i.e., solutions where the absolute values of the elements of $\boldsymbol{J}_{ion}$ are small. If, in turn, we define $\boldsymbol{D}$ as $\boldsymbol{D}_1$, the first derivative operator, solutions that tend toward constant values of $\boldsymbol{J}_{ion}$ would be favored (small first derivative).

[26] Note that we can also calculate the expected covariance of the solution, $\boldsymbol{\sigma}_J^2$ through the relationship [*Menke*, 1989]

$$\boldsymbol{\sigma}_J^2 = \boldsymbol{G}\boldsymbol{\sigma}_C^2\boldsymbol{G}^T, \tag{27}$$

defining the generalized inverse $\boldsymbol{G}$ from equation (25) as

$$\boldsymbol{G} \equiv \left(\boldsymbol{K}^T\boldsymbol{\sigma}_C^{-2}\boldsymbol{K} + \gamma\boldsymbol{H}\right)^{-1}\boldsymbol{K}^T\boldsymbol{\sigma}_C^{-2}. \tag{28}$$

We must now determine the best γ and $\boldsymbol{H}$ to use with the HENA data.

5.2. Constraint Matrices

[27] As we have pointed out earlier, the HENA measurements do not contain enough information to unambiguously determine the ion distribution, J_{ion}. The added information takes the form of an a priori assumption that along with minimizing the expression in equation (22) the best solutions will also minimize the quantity $\boldsymbol{J}_{ion}^T\boldsymbol{H}\boldsymbol{J}_{ion}$. In this section we will introduce specific forms of the constraint matrix $\boldsymbol{H}$ that will subsequently be evaluated for applicability to the HENA data.

[28] It should be pointed out that in the absence of constraints, the estimated $\boldsymbol{J}_{ion}$ oscillates rapidly between unreasonable large positive values and large negative (and therefore completely unphysical) values. In a certain sense the constraints serve to damp this oscillation. The simplest constraint would favor smaller values of $\boldsymbol{J}_{ion}$ and reject larger ones. As we have pointed out before, the identity matrix $\boldsymbol{H}_0 = \boldsymbol{D}_0^T\boldsymbol{D}_0 = \boldsymbol{I}$ serves this purpose well. The drawback, of course, is that this constraint will tend to force the solution to be smaller than it should be.

[29] We can also damp the oscillations in $\boldsymbol{J}_{ion}$ by requiring the solution to be smooth rather than small. For this purpose we choose a slightly modified version of the second derivative operator, i.e., the Laplacian, in the construction of $\boldsymbol{J}$ via equation (26). The equatorial (L, ϕ) is a cylindrical coordinate system so the modified second derivative operator is written

$$\nabla^2 = \frac{\partial^2}{\partial r^2} + \frac{1}{r}\frac{\partial}{\partial r} + \alpha\frac{1}{r^2}\frac{\partial^2}{\partial\phi^2}, \tag{29}$$

where we have introduced the asymmetry parameter α, which can be used to adjust the smoothness more strongly in either the L or ϕ direction. This free parameter α is introduced because we have no a priori reason to expect an equal amount of smoothness in L and ϕ. We implement equation (29) using a second-order finite difference stencil. Two other modifications are required before this constraint can be used. First, the boundary in ϕ is cyclical; thus the finite difference stencil must be modified to calculate the proper derivatives across the boundary at each L. Second, we require that the ion distribution be small at the boundaries in L. We implement this "clamping" by replacing the smoothness constraint for the minimum and maximum L with the identity constraint. We can thus express the smoothness constraint as

$$\boldsymbol{H}_2(\alpha,\lambda) = \boldsymbol{D}_2^{*T}(\alpha)\boldsymbol{D}_2^{*}(\alpha) + \lambda\boldsymbol{H}_0^b, \tag{30}$$

where $\boldsymbol{D}_2^{*}(\alpha)$ is the modified second derivative operator, $\boldsymbol{H}_0^b$ is the $\boldsymbol{H}_0$ operator that acts only on the L boundaries, and λ is used to adjust the relative strength of the clamping constraint. The $\boldsymbol{H}_2$ constraint favors solutions with small spatial second derivatives, that is, solutions that increase or decrease linearly.

[30] Instead of the more mathematically constructed constraints above, we could take a more physically based approach, making the straightforward assumption that elements of $\boldsymbol{J}_{ion}$ that lie close to one another are more closely correlated to one another than elements that are widely spatially separated. This type of constraint has been described by *Rodgers* [2000], who relates its construction to a Markov-type process. The two dimensional Markov constraint matrix has elements

$$\boldsymbol{H}_m^{ij} = e^{-d_{ij}/d_m}, \tag{31}$$

where d_{ij} is the Euclidian distance between element (L_i, ϕ_i) and (L_j, ϕ_j) and d_m is an adjustable parameter that describes the characteristic length of the covariance. In the construction of d_{ij} we implement the cyclical boundary in ϕ. We also add the clamping constraint at the boundaries, so that the Markov constraint is most properly expressed as $\boldsymbol{H}_m(d_m, \lambda)$. Note that in the limit of small d_m, the Markov constraint becomes identical to the identity constraint (when properly normalized). As d_m increases, the correlation between neighboring points increases, and the constraint tends to favor solutions where the covariance weighted mean around any given point is smaller. Like the identity constraint, the Markov constraint will tend to force the solution to be smaller than it should be. We now proceed to describe

methods for selecting constraints and optimizing their free parameters.

5.3. Method for Tuning the Constraints

[31] Clearly, the optimal choice of γ, $\boldsymbol{H}$, and the free parameters of $\boldsymbol{H}$ should yield a solution that is both consistent with the measurement and reflective of the underlying ion distribution. Consistency with the measurement can be easily quantified via the expression (22). For this purpose we define the goodness of fit, g_f, as

$$g_f(\boldsymbol{p}_H) = \frac{1}{n_C}(\boldsymbol{C} - \boldsymbol{K}\boldsymbol{J}_{ion})\boldsymbol{\sigma}_C^{-2}(\boldsymbol{C} - \boldsymbol{K}\boldsymbol{J}_{ion}), \tag{32}$$

where n_C is the number of measurements (i.e., the number of pixels in the HENA image) and $\boldsymbol{p}_H$ is the appropriate array of constraint parameters (γ for $\boldsymbol{H}_0$, (γ, α, λ) for $\boldsymbol{H}_2$, and (γ, d_m, λ) for $\boldsymbol{H}_m$). We expect g_f to be approximately 1 for a retrieved ion distribution that is consistent with the data.

[32] For real measurements it is not possible to gauge how well the solution reflects the underlying ion distribution. We can, however, simulate images from a representative ion distribution that would produce an ENA image with a morphology similar to the observed image, use equation (24) to estimate ion distribution from this image and then compare the given ion distribution to the estimated ion distribution. Following this process, we can define the goodness of the retrieval, g_r, as

$$g_r(\boldsymbol{p}_H) = \frac{1}{n_J}\left(\boldsymbol{J}^0_{ion} - \boldsymbol{J}_{ion}\right)\boldsymbol{\sigma}_J^{-2}\left(\boldsymbol{J}^0_{ion} - \boldsymbol{J}_{ion}\right), \tag{33}$$

where n_J is the number of elements of $\boldsymbol{J}_{ion}$ and $\boldsymbol{J}^0_{ion}$ is the ion distribution used for the image simulation. We have chosen to simulate the images using the the parameterization of *Roelof and Skinner* [2000]. In doing so, the quantity g_r reflects the systematic errors incurred in linearizing the problem (since *Roelof and Skinner* [2000] use a nonlinear, direct integration method). After the simulated image is constructed, gaussian noise that is consistent with the pixel rates in the measured image is added. In order to do so, the simulated image is scaled so that the maximum simulated pixel is equal to the maximum measured pixel, and then uncertainties consistent with counting statistics are assumed for the scaled simulated image.

[33] We expect that for an acceptable solution, g_r should be approximately 1. If g_r is significantly greater that 1, the retrieved ion density, $\boldsymbol{J}_{ion}$ differs too greatly from the input ion density $\boldsymbol{J}^0_{ion}$. If in turn, g_r is significantly less than 1, the covariance of the retrieved values, $\boldsymbol{\sigma}_J^2$ is too large, i.e., the uncertainty of $\boldsymbol{J}_{ion}$ can be made smaller through tightening the constraints.

[34] If we regard both g_r and g_f as functions of the constraints, we can determine a set of acceptable constraints for a particular observation geometry by minimizing the quantity

$$q(\boldsymbol{p}_H) \equiv (1 - g_r(\boldsymbol{p}_H))^2 + \left(1 - g_f(\boldsymbol{p}_H)\right)^2 \tag{34}$$

for a simulated image similar in character to the actual measurements. When this quantity is made small, we are assured that for the simulated image, the retrieval is both reflective of the assumed underlying ion distribution and consistent with the input image. The constraints so determined then can be used with the actual measurements and expected to similarly retrieve the actual underlying ion distribution.

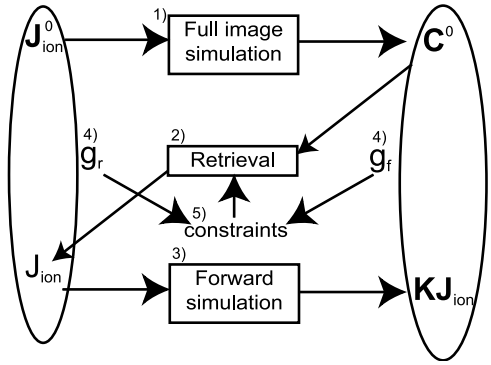

Figure 4. Method of constraint tuning. (1) An assumed ion distribution $\boldsymbol{J}^0_{ion}$ is used to create a simulated image, $\boldsymbol{C}^0$ via the full integration method of *Roelof and Skinner* [2000]. (2) An ion distribution, $\boldsymbol{J}_{ion}$ is retrieved from the simulated image using an initial guess for the constraints. (3) An image, $\boldsymbol{K}\boldsymbol{J}_{ion}$ is reconstructed from the retrieved ion density. (4) The goodness of fit and retrieval, g_f and g_r are calculated from $\boldsymbol{K}\boldsymbol{J}_{ion}$ and $\boldsymbol{J}_{ion}$. (5) The constraints are modified based on g_f and g_r. The process resumes at step 2 using the new constraints and continues until the quantity q is minimized.

5.4. Example Tuning and Error Analysis

[35] Our method for minimizing q and therefore optimizing the constraints are shown in Figure 4. The constraints are adjusted to minimize the quantity q by means of a nonlinear simplex minimization given by *Press et al.* [1988].

[36] Thus for a given form of $\boldsymbol{H}$, we can systematically select the constraint parameters, $\boldsymbol{p}_H$, that optimally retrieve a test image. We then assert that if we are given an image that is similar in character to the test image, this set of constraint parameters will be suitable. In this case, similar in character implies a similar viewing geometry, similar signal to noise ratio and a qualitatively similar ion distribution.

[37] The HENA instrument acquires images with very disparate viewing geometries and ENA intensities; for this reason it is difficult to provide a comprehensive assessment of the quality of our inversion algorithm. The tuning process described above, however, provides information on how well the inversion process should be expected to work for a particular measurement. In this section, we examine the application of the tuning process and the quality of the retrieval for a particular image that is reasonably representative of much of the HENA data.

[38] Our analysis focuses on the image shown in Figure 5, on which the simulation shown in Figure 3 was based. Note that the image in Figure 5 features a peak on the dawn side of midnight, rather than the dusk side of midnight as appears in the simulation. Also the measured emission is less intense at the peak than in the simulation. Because the signal to noise ratio is higher for brighter emission, the

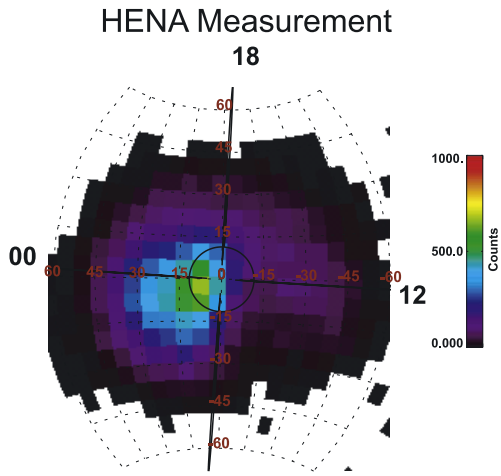

Figure 5. HENA image from 4 October 2000 displayed in the same format as Figure 3.

uncertainties in the simulated image must be scaled accordingly to be representative of the measured data. This process of scaling is described above.

[39] The full nonlinear simulation (using the model from *Roelof and Skinner* [2000] as described above) with the appropriate noise added is shown in Figure 6. This image employs the same ion distribution as the one used in Figure 3. As is to be expected, the principle difference between Figure 6 and Figure 3 is addition of noise.

[40] The results of the tuning process and a summary of the dependence of the tuning measurements, g_f, g_r and q, on the constraint strength, γ, are shown in Figure 7. Before examining the details of the retrievals themselves, we will first discuss the general behavior of the tuning process shown in the right column of the figure.

[41] The qualitative behavior of the various tuning measurements, g_f, g_r, and q, as a function of the constraint strength, γ, is similar for all of the constraint types. At small values of γ, the quality of the fit, g_f, is close to one, as the constraints merely push the retrieval away from the mathematically optimal retrieval (which oscillates wildly) towards a more physically realistic one. As γ increases, g_f climbs away from one, and the retrieval becomes more and more biased towards the constraint. The quality of the retrieval, g_r, also monotonically increases as a function of γ, though at small values of γ it is significantly less than one. This is not because the retrieved ion distribution faithfully reproduces the test ion distribution, rather, it is because the retrieved covariance is very large when γ is small. As γ grows, the covariance shrinks and g_r increases. For this reason it is important to regard g_r as a measure of the fidelity of the retrieval with respect to the estimated uncertainty of the retrieval. Thus an optimized retrieval will always be reasonably accurate in a formal sense (taking the retrieval and the uncertainty both into account), however the uncertainties may be so large that the retrieval has very limited utility.

[42] We observe that though each of the constraints tested exhibited a deep minimum in q, the resulting ion distributions vary somewhat. We will consider each constraint type in turn.

[43] The identity constraint, H_0, is by far the simplest constraint to implement and optimize. In this case q can be regarded as a simple function of the constraint strength, γ, and a one-dimensional optimization can be carried out. In practice, as can be seen in Figure 7, this constraint also provides a reasonable retrieval. Clearly, the peak intensity is underestimated, however the morphology of the ion distribution is accurately reproduced. The underestimation of the peak is not unexpected, as the identity constraint tends to force the retrieval to smaller values. It is important to take into account the contours of constant relative uncertainty in the figure. From these contours it is clear that although the morphology of the ion distribution is produced quite well away from the peak value, it is quantitatively unreliable. Further, even near the peak value there are only a few pixels whose relative uncertainty is less than 50%.

[44] The second derivative constraint, H_2, yields what appears at first glance to be a different retrieval. The retrieval near the peak is faithfully reproduces the input ion distribution. Further, the number of pixels with less than 50% relative error has increased. This favorable behavior near the peak is offset by rather poor behavior away from the peak. A spurious second peak in the dawn-noon sector has appeared. This is mitigated by the relative uncertainties, which are rather large in this region. If the uncertainties are taken into account, the H_2 constraint yields a reasonable retrieval, particularly in the region of the peak intensity, however the behavior in the less well determined areas is undesirable.

[45] The Markov constraint, H_m, yields a retrieval that is similar in character to the identity constraint, H_0. This is not surprising, as the optimal characteristic length, d_m, is fairly small (0.109) and thus has only small off-diagonal elements, and therefore H_m is very similar to H_0. The retrieval with the H_m constraint is, however, preferable to the retrieval with the H_0 constraint. The magnitude of the peak is still underestimated, but to a lesser extent than the H_0 constraint. The range where the uncertainties are less than 50% is similar to that of the H_2 retrieval, and the morphology off-peak is

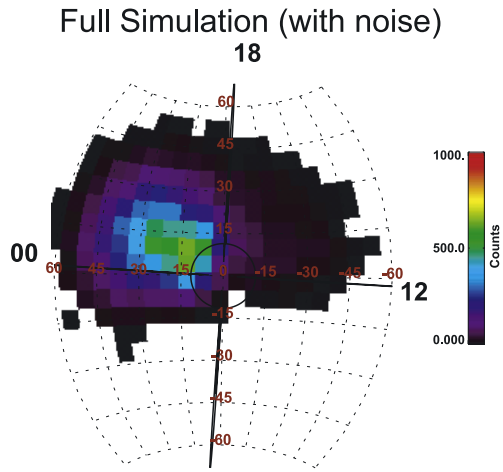

Figure 6. Full nonlinear simulation using the ion distribution in Figure 3 and the image geometry of Figure 5 with noise added.

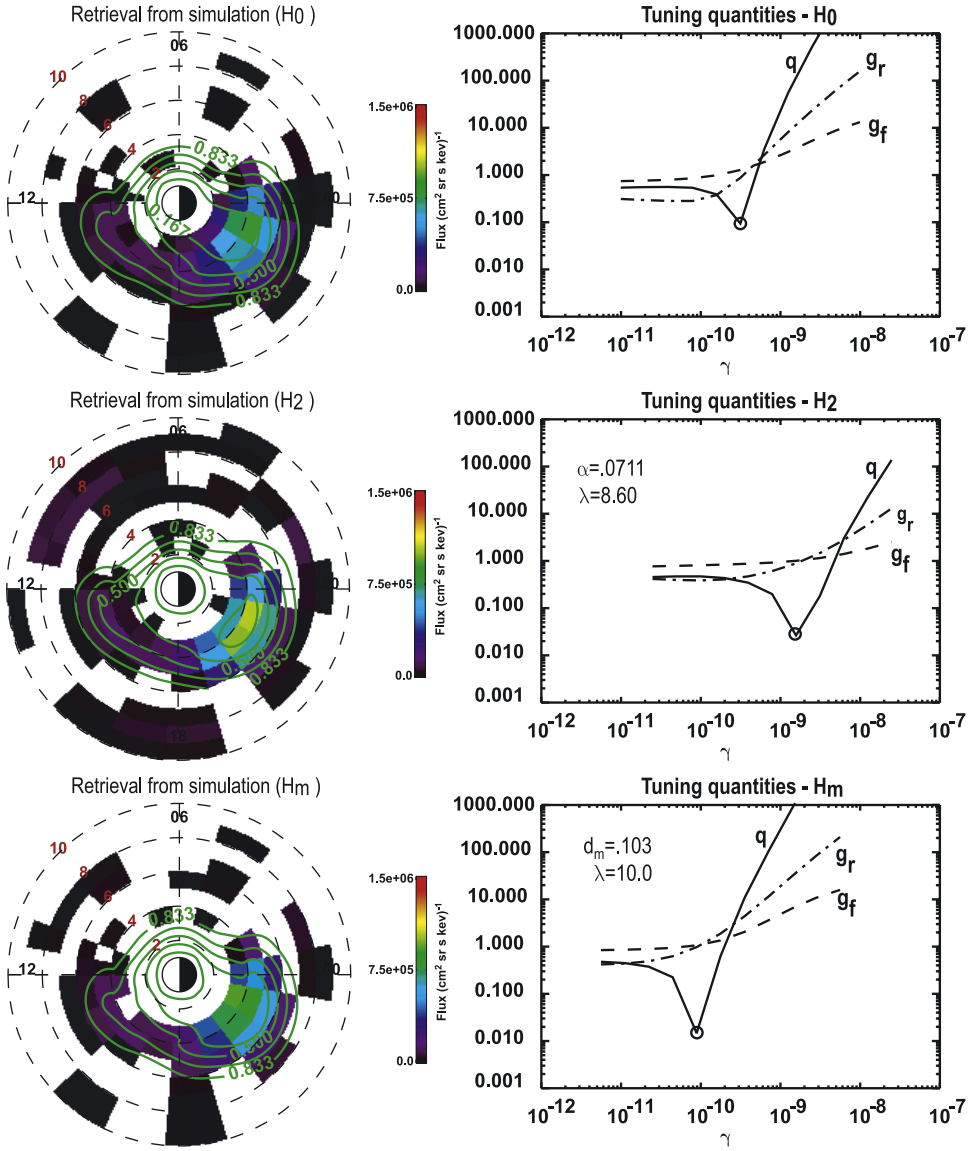

Figure 7. Optimal retrievals and tuning quantities for various constraint types. Optimized retrievals of the simulated image in Figure 6 for the three constraint types, H_0, H_2, and H_m are shown on the left. The plots on the right show the various tuning measures (g_f, g_r, and q) as a function of the constraint strength γ. The images on the left are rendered on the same scale as the ion distribution in Figure 3 and can be compared with this figure directly. Contours of relative uncertainties are also shown on the ion distribution images. The plots on the right were made for the optimal values of the additional tuning parameters (α, λ, and d_m); The value of these parameters are also shown on the plot. The minimum value of q at the optimal γ are circled in each plot.

more representative. The behavior of the retrieval near the outer L boundary has somewhat less noise than the H_0 retrieval, no doubt because of the introduction of the boundary clamping parameter λ.

[46] Clearly, choosing the constraints is a somewhat subjective enterprise. Different constraints will enhance some aspects of the retrieval at the expense of other aspects. This is clear from the discussion above in regard to the differences between the H_0 and H_m constraints. If we wish to be as careful as possible in the region of the emission peak, we should choose to use the H_2 constraint. If, however, we wish to better reproduce global morphology, the H_m constraint is preferable. We have found this relationship between the H_m and H_2 to exist in simulations of most viewing geometries, ion distribution morphologies, and magnitudes.

[47] We have also found that the H_m constraint yields retrievals that are less sensitive to variation in the underlying ion distributions, particularly where the Earth blocks the viewing of some areas of local time. In order to demonstrated this, we tuned a retrieval for a given ion distribution for both constraint types. We then used the tuning parameters, $\boldsymbol{p}_H$, that resulted to retrieve simulated images using a many different underlying ion distributions. Using the tuning measures g_f, g_r and q, we found that the H_m retrievals were generally more reliable. As a result, we

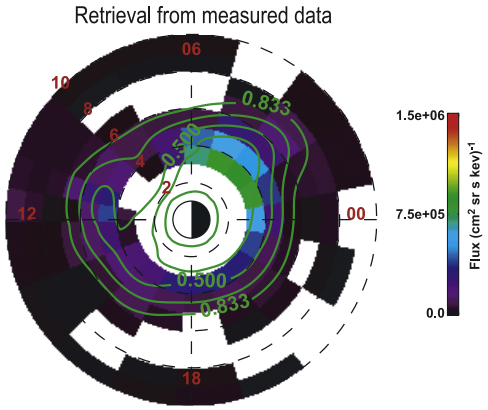

Figure 8. Retrieval results for the image in Figure 5 using the optimal H_m constraints shown in Figure 7. The color scale and legend are the same as in Figure 7.

have developed a double tuning process, which we have found to be quite useful. We begin by tuning the observation with the above process using a simulated ion distribution and the H_m constraint. The results of the tuning are then used in a retrieval of the observed image, yielding an ion distribution. We then use the resulting ion distribution as input to a second tuning process using the H_2 constraint. The resulting parameters are then used on the image. The first stage retrieval is designed to reproduce the morphology correctly; the second stage uses this morphology to yield a better quantitative retrieval.

[48] Before concluding, we present the results of the retrieval using the data (Figure 5) on which the above optimization was based. The results of the retrieval using the H_m constraint (using the optimal parameters) are shown in Figure 8. The retrieval shows quantitatively some of the features that we surmised when comparing the simulated and actual emissions (Figures 6 and 5, respectively).

6. Summary and Conclusions

[49] In this work we have developed a technique for the retrieval of global magnetospheric ion densities from high-energy neutral atom measurements from the HENA instrument. The basic equations governing the HENA measurements were summarized. The HENA response function is also explicitly included in our treatment. After presenting the equations of measurement, simulations based on these equations were shown and their important features described. We then turned to developing the retrieval technique. It is noted that the retrieval of ion distributions is an ill-posed problem, i.e., it has not unique solution. For this reason, we described the introduction of constraints and a quantitative method of determining what they should be. Finally, we calculated optimal constraints for a representative HENA image and performed retrievals on simulated data in order to explore the reliability of the retrievals.

[50] In short, we have developed a retrieval technique and provided a means of quantifying its fidelity. We have also applied these to a representative image and shown that these techniques are indeed useful for determination of ion densities. Without this or a similar method of retrieval, only qualitative conclusions can be drawn from the ENA images about the source ion distribution. The retrievals are only as good as our knowledge of the instrument.

[51] There are several ways in which these techniques can be improved. First, much work has yet to be done on refining the constraints. We have presented some very simple examples of how these retrievals can be constrained. A more sophisticated treatment, e.g., one that has a strong physical basis, may yield a significant increase in the quality of the retrievals. Second, in the absence of extremely high count rates (i.e., unless the signal to noise ratio is very high) we can only poorly quantify the pitch angle distribution of the ions. We intend to approach this problem by combining the information in images taken at multiple viewpoints. Early attempts at this have been encouraging, and a detailed study is underway. Third, the retrieval equations are based on a simple dipole magnetic field. This may lead to errors particularly at higher values of L. We are currently seeking a method of incorporating a more realistic magnetic field without prohibitively increasing the computational cost.

Appendix A: Linear Quadratures

[52] The approximation of double integrals by numerical quadratures is an important element in the techniques developed above. In short, we wish to find an approximation of the form

$$\sum_{k=1}^{N}\sum_{l=1}^{M} b_{kl} f(x_k, y_l) \cong \int_{a_x}^{b_x}\int_{a_y}^{b_y} K(x,y) f(x,y)\,dx\,dy, \qquad \text{(A1)}$$

where $K(x, y)$ is some known function, $f(x, y)$ is a continuous function that can be sampled at $N \times M$ points $f(x_k, y_l)$ and b_{kl} are weights which will now be developed.

[53] In order to formulate the approximation in equation (A1), some assumption about the behavior of $f(x, y)$ between the quadrature points, $f(x_k, y_l)$, must be assumed. In the simplest case we assume that $f(x, y)$ remains constant around each grid point and $f(x_k, y_l)$ is given on a regular grid with separations Δx, Δy. In this case we obviously have $b_{kl} = \Delta x \Delta y$. A more robust technique would assume some functional dependence of $f(x, y)$ between the quadrature points. The success of the quadrature scheme depends on the accuracy of such an assumption.

[54] In this work, we adapt a one-dimensional linear quadrature technique presented by *Twomey* [1977] and briefly summarized here. In the one dimensional version of the problem, we seek an approximation to the integral of the form

$$\sum_{j=1}^{N} b_j f_j \cong \int_a^b K_1(x) f_1(x)\,dx \qquad \text{(A2)}$$

The integral may be broken up into intervals

$$\int_a^b K_1(x) f_1(x)\,dx = \sum_{j=1}^{N} \int_{x_j}^{x_{j+1}} K_1(x) f_1(x)\,dx \qquad \text{(A3)}$$

If we assume that the function $f(x)$ is linear in each subinterval, we can write

$$\int_a^b K_1(x) f_1(x) dx = \sum_{j=1}^{N-1} \int_{x_j}^{x_{j+1}} K_1(x)\left(A_j + B_j x\right) dx, \tag{A4}$$

where A_i and B_i are constants determined by the $2 \times (N-1)$ equations

$$\begin{aligned} f\left(x_j\right) &= A_j + B_j x_j \\ f\left(x_{j+1}\right) &= A_j + B_j x_{j+1}. \end{aligned} \tag{A5}$$

If these equations are solved in terms of the $f(x_j)$, the result substituted into equation (A4) and placed in the form of equation (A2), the final expression for the quadrature weights, b_j becomes

$$\begin{aligned} b_j &= \frac{\varphi_{j-1}^1 - x_{j-1}\varphi_{j-1}^0}{x_j - x_{j-1}} + \frac{x_{j+1}\varphi_j^0 - \varphi_j^1}{x_{j+1} - x_j}, \quad 2 \le j \le N-1 \\ b_1 &= \frac{x_2\varphi_1^0 - \varphi_1^1}{x_2 - x_1} \\ b_N &= \frac{\varphi_{N-1}^1 - x_{N-1}\varphi_{N-1}^0}{x_N - x_{N-1}}, \end{aligned} \tag{A6}$$

where the moments φ_j^m are

$$\varphi_j^m = \int_{x_j}^{x_{j+1}} x^m K_1(x) dx. \tag{A7}$$

Thus the one dimensional quadrature weights in equation (A2) can be expressed through the moments of the function $K_1(x)$ over the subintervals (x_j, x_{j+1}).

[55] The two-dimensional analog of the one-dimensional quadrature can be derived through repeated application of equation (A6). This process results in the two-dimensional quadrature weights b_{kl} from equation (A1)

$$b_{kl} = \sum_{m=0}^{1} \sum_{n=0}^{1} \zeta_{(k+m-1)(l+n-1)}^{m,n}, \tag{A8}$$

where

$$\begin{aligned} \zeta_{kl}^{nm} &= \int_{x_l}^{x_{l+1}} \int_{y_k}^{y_{k+1}} g_{kl}^{nm} f dx dy \quad \text{if} \quad \begin{matrix} 1 \le k \le N-1 \\ 1 \le l \le M-1 \end{matrix} \\ \zeta_{kl}^{nm} &= 0 \quad \text{otherwise} \end{aligned} \tag{A9}$$

and

$$g_{kl}^{nm} = \frac{(-1)^{n+m}(x_{l+m} - x)(y_{k+n} - y)}{(x_{l+1} - x_l)(y_{k+1} - y_k)}. \tag{A10}$$

Thus we have derived a numerical approximation for equations of the form (A1). This approximation is accurate when the function $f(x, y)$ in equation (A1) can be approximated by a bilinear function.

[56] **Acknowledgments.** This work was supported under NASA contract NAS5-96020 through subcontract with the Southwest Research Institute and NASA grant NAG5-12772. We gratefully acknowledge helpful conversations with Jeng-hwa Yee. This work is part of the dissertation research of R. DeMajistre at the School of Computational Sciences at George Mason University, Fairfax, Virginia.

[57] Lou-Chuang Lee thanks Jerry Goldstein and the other reviewer for their assistance in evaluating this paper.

References

Abramowitz, M., and I. Stegun (1972), *Handbook of Mathematical Functions*, Dover, Mineola, N.Y.

Barnett, C. F. (1990), Collisions of H, H_2, He, and Li atoms and ions with atoms and molecules, in *Atomic Data for Fusion*, *ORNL-6086*, vol. 1, Control. Fusion Atomic Data Cent., Oak Ridge Natl. Lab., Oak Ridge, Tenn.

C:son Brandt, P., R. Demajistre, E. C. Roelof, D. G. Mitchell, and S. Mende (2002), IMAGE/HENA: Global ENA imaging of the plasmasheet and ring current during substorms, *J. Geophys. Res.*, *107*(A12), 1454, doi:10.1029/2002JA009307.

Gibson, W. C., et al. (2000), The image observatory, *Space Sci. Rev.*, *91*, 15–50.

Lyons, L., and D. Williams (1984), *Quantitative Aspects of Magnetospheric Physics*, D. Reidel, Norwell, Mass.

Menke, W. (1989), *Geophysical Data Analysis: Discrete Inverse Theory*, Academic, San Diego, Calif.

Mitchell, D. G., et al. (2000), High energy neutral atom (HENA) imager for the IMAGE mission, *Space Sci. Rev.*, *91*, 67–112.

Østgaard, N., S. B. Mende, H. U. Frey, G. R. Gladstone, and H. Lauche (2003), Neutral hydrogen density profiles derived from geocoronal imaging, *J. Geophys. Res.*, *108*(A7), 1300, doi:10.1029/2002JA009749.

Perez, J. D., M.-C. Fok, and T. E. Moore (2000), Deconvolution of energetic neutral atom images of the earth's magnetosphere, *Space Sci. Rev.*, *91*, 421–436.

Perez, J. D., G. Kozlowski, P. C. Brandt, D. G. Mitchell, J. M. Jahn, C. J. Pollock, and X. Zhang (2001), Initial ion equatorial pitch angle distributions from energetic netural atom images obtained by IMAGE, *Geophys. Res. Lett.*, *28*, 1155–1158.

Press, W., B. Flannery, S. Teukolsky, and W. Vetterling (1988), *Numerical Recipes in C*, Cambridge Univ. Press, New York.

Rairden, R. L., L. A. Frank, and J. D. Craven (1986), Geocoronal imaging with dynamics explorer, *J. Geophys. Res.*, *91*, 13,613–13,630.

Rodgers, C. (2000), *Inverse Methods for Atmospheric Sounding*, World Sci., River Edge, N. J.

Roelof, E. C. (1987), Energetic neutral atom image of a storm-time ring current, *Geophys. Res. Lett.*, *14*, 652–655.

Roelof, E. C., and A. J. Skinner (2000), Extraction of ion distributions from magnetospheric ENA and EUV images, *Space Sci. Rev.*, *91*, 437–459.

Russell, C. T. (1971), Geophysical coordinate transformations, in *Cosmic Electrodynamics*, vol. 2, pp. 184–196, D. Reidel, Norwell, Mass.

Twomey, S. (1977), *Introduction to the Mathematics of Inversion in Remote Sensing and Indirect Measurements*, Elsevier Sci., New York.

Vallat, C., et al. (2004), First comparisons of local ion measurements in the inner magnetosphere with energetic neutral atom magnetospheric image inversions: Cluster-CIS and IMAGE-HENA observations, *J. Geophys. Res.*, *109*, doi:10.1029/2003JA010224, in press.

P. C:son Brandt, R. DeMajistre, E. C. Roelof, and D. G. Mitchell, Applied Physics Laboratory, Johns Hopkins University, 11100 Johns Hopkins Road, Laurel, MD 20723, USA. (pontus.brandt@jhuapl.edu; robert.demajistre@jhuapl.edu; edmond.roelof@jhuapl.edu; donald.g.mitchell@jhuapl.edu)